Available online at www.sciencedirect.com
SCIENCE DIRECT®
Computational Materials Science 34 (2005) 221–234
COMPUTATIONAL MATERIALS SCIENCE
www.elsevier.com/locate/commatsci

Crystal plasticity simulation study on the influence of texture on earing in steel

D. Raabe [a,*], Y. Wang [b], F. Roters [a]

[a] *Max-Planck-Institut für Eisenforschung, Max-Planck-Straße 1, D-40237 Düsseldorf, Germany*
[b] *Department of Metallurgical Engineering, University of Missouri-Rolla, MO 65409-0340, USA*

Received 3 August 2004; received in revised form 23 November 2004; accepted 10 December 2004

Abstract

We present a numerical study on the influence of crystallographic texture on the earing behavior of a low carbon steel during cup drawing. The simulations are conducted by using the texture component crystal plasticity finite element method which accounts for the full elastic–plastic anisotropy of the material and for the explicit incorporation of texture including texture update. Several important texture components that typically occur in commercial steel sheets were selected for the study. By assigning different spherical scatter widths to them the resulting ear profiles were calculated under consideration of texture evolution. The study reveals that 8, 6, or 4 ears can evolve during cup drawing depending on the starting texture. An increasing number of ears reduces the absolute ear height. The effect of the orientation scatter width (texture sharpness) on the sharpness of the ear profiles was also studied. It was observed that an increase in the orientation scatter of certain texture components entails a drop in ear sharpness while for others the effect is opposite.

PACS: 62.20.Fe; 46.15.Cc; 46.90; 45.10.Db

Keywords: Plastic deformation; Anisotropy; Modeling; Earing; Body-centered-cubic; Sheet forming; Springback; Deep drawing

1. Introduction

1.1. Integration of plastic anisotropy into metal forming simulations

The shape anisotropy of cup drawn metallic parts is referred to as earing. It is a characteristic phenomenon associated with the crystallographic

* Corresponding author. Tel.: +49 211 6792 278; fax: +49 211 6792 333.
E-mail address: raabe@mpie.de (D. Raabe).

0927-0256/$ - see front matter © 2005 Elsevier B.V. All rights reserved.
doi:10.1016/j.commatsci.2004.12.072

texture and the resulting elastic–plastic anisotropy of metals [1–16]. Sheet steels usually have pronounced textures which they inherit from the preceding processing steps such as hot rolling, cold rolling, and heat treatment [17–23].

Various concepts exist to introduce texture-related sheet anisotropy into finite element models for sheet forming. The initial material anisotropy existing before sheet deformation can be incorporated either through an anisotropic yield surface function or directly via the incorporation of crystallographic texture models into the finite element codes. The anisotropic yield surface models can be classified into two groups. The first one comprises empirical and phenomenological anisotropic yield surface equations, such as the equations of Hill from 1948 [24] and 1979 [25], Hosford [26], Barlat [27], or Barlat and Lian [28] to name but a few important ones. These yield surface functions are formulated as convex higher-order polynoms, i.e. they take an empirical view at plastic anisotropy. The physical nature of anisotropy can be incorporated into these concepts for instance by fitting the corresponding polynomial coefficients with the aid of texture-based strain-rate or self-consistent homogenization methods or with anisotropy parameters obtained from mechanical tests. A detailed overview of this class of yield surface concepts was recently given by Banabic et al. [29]. The second type of yield surface models is directly formulated as texture-based yield loci [30–34] the coefficients of which can be directly expressed in terms of the texture-based mechanical models in conjunction with experimentally determined orientation distributions.

The advantage of yield surface concepts for mechanical anisotropy predictions are relatively short calculation times, when implemented into finite element models, although one must recall that the measurement of the mechanical anisotropy parameters and the fitting of the anisotropy coefficients must be added to the total time required for a prediction.

The main disadvantage of the yield surface concept is that they do not consider that the inherited sheet starting textures may evolve further in the course of sheet forming. This means that reliable anisotropy simulations should incorporate the starting texture as well the gradual *update* of that texture during deep drawing operations [35]. Some recent results indeed indicate that the change in crystallographic texture during deep drawing may be relevant for the resulting ear shapes [11,16].

In order to take into account texture evolution during deformation, the crystallographic texture models have been developed. These models can be roughly classified into three groups, namely, combinations of a Taylor-type strain-rate homogenization model and finite element formulations, the crystal plasticity finite element model, and texture-function based crystal plasticity finite element models.

The approach of combining a Taylor model with a finite element model was introduced by Gottstein and coworkers [36–39]. In this approach the deformation tensor after each strain increment is used to prescribe the boundary conditions for a corresponding Taylor simulation using full constraints or coupled full constraints/grain interaction homogenization model. Each of the finite elements contains its representative crystallographic texture information in the form of a large set of discrete grain orientations. The Taylor factor calculated from homogenization is fed back into the finite element simulation as a correction factor for the flow stress in the ensuing simulation step. The particular strength of this method lies in the exact simulation of texture evolution under intricate boundary conditions.

The crystal plasticity finite element models consist in a direct implementation of crystallographic slip kinematics into finite element models. It was first suggested by Peirce and co-workers [39–42]. Based on their early work a fully-implicit time-integration scheme was developed by Kalidindi et al. [43] and implemented in commercial finite element software in the form of a user-defined subroutine. Crystal plasticity finite element models provide a direct means for updating the material state via integration of the evolution equations for the crystal lattice orientation and the critical resolved shear stress. The deformation behavior of the grains is at each integration point determined by a crystal plasticity model, which accounts for plastic deformation by crystallographic slip and

for the rotation of the crystal lattice during deformation. Pioneering related studies along these lines have been published by Mathur and Dawson [44], Smelser and Becker [45], and Beaudoin et al. [46]. Crystal plasticity finite element models represent elegant tools for detailed simulation studies of texture evolution under realistic boundary conditions. Each integration point can represent one single orientation or even a large set of discrete grain orientations when combined with an appropriate homogenization assumption. Although the latter case (mapping of a representative texture on one integration point) is principally feasible, it entails long calculation times, rendering the method less practicable for industry-scale applications.

For rendering the crystal plasticity finite element models more flexible with respect to the treatment of large polycrystalline entities Raabe and Roters recently introduced a texture component crystal plasticity finite element model [47,48]. The basic idea of this method consists in using a more effective way of describing the texture of macroscopic samples at each integration point, turning the method into a texture component crystal plasticity finite element method. More details on this approach are given in the ensuing section.

1.2. Previous simulation studies on earing of body centered cubic steels

Only few systematic simulation studies were published on the earing behavior of body-centered-cubic steels. For instance, Bacroix and Gilormini [3] presented a detailed work on earing in polycrystalline materials by use of finite-element simulations. They used a texture-adjusted fourth-order strain-rate potential and its associated normality rule. The coefficients of the potential function were directly obtained from the texture coefficients. They applied the method successfully to a mild steel. The approach was capable of reproducing six ears for certain textures. Li et al. [33,38] predicted the earing behavior of cup drawn IF (interstitial free) steel sheets by use of a texture-based plastic potential formulation. The group of Nakamachi et al. [49,50] used an elastic–viscoplastic finite element method to simulate the six and four ears of drawn cups of body centered cubic polycrystals. In order to achieve this goal they used a large number of integration points in conjunction with a crystal plasticity finite element formulation. Each rotation matrix mapped at an integration point was assumed to represent one grain. The crystallites could hence rotate individually upon mechanical loading. The sheet metal forming simulations of Nakamachi et al. [49,50] were not only used to predict the earing behavior but also to assess texture effects on strain localization and failure. The authors reported that $\{1\,1\,1\}\langle u\,v\,w\rangle$ orientations (γ-fiber texture) are favorable while the $\{h\,k\,l\}\langle 0\,0\,1\rangle$ texture components where less favorable for sheet formability of steels.

These studies provide in part excellent insight into the relationship between the initial crystallographic texture of steel sheets before cup drawing and the resulting ear profiles after deformation. Building on these observations the present study aims at pushing this effort a step further by, first, rigorously incorporating texture update into the simulations according to the crystal plasticity scheme, second, by a systematic variation of the relevant texture components typically occurring in body-centered-cubic steels [22,23], and third, by systematically varying the orientational scatter width of those texture components. The simulations are conducted by using the texture component crystal plasticity finite element model. After an introduction to this method and to the model set-up we simulate the individual ear profiles resulting from some typical texture components of body-centered-cubic polycrystals. Subsequently, we discuss the effects of these texture components on the observed ear profiles and also the effects of changes in the scatter width of these textures on the ear profile.

2. The texture component crystal plasticity finite element method

2.1. Introduction to the simulation method

A challenge of integrating constitutive polycrystal plasticity laws into finite element approaches lies in identifying an effective method of mapping a crystallographic texture which represents a *large*

number of grains on the integration points of a finite element mesh. Such an approach must be formulated in a way that still permits texture update in the course of the forming simulation.

It is an important condition in that context that crystal plasticity finite element models require a *discrete* representation of the orientation distribution function at each integration point. For relatively small numbers of grains (less than 10^3 crystals) the discrete mapping of the texture on the mesh can be achieved by a one-to-one approach, where each Gauss point in the finite element grid is characterized by one crystallographic orientation [49–51]. This method, however, is not suitable when meshing specimens which contain a much large number of grains such as in a typical steel sheet which is subjected to large scale metal forming operations.

2.2. Texture components

The texture component finite element method is a novel approach in the context described above [16,47,48]. It is a technique of approximating an initial orientation distribution function in the form of discrete sets of symmetrical spherical model functions and in mapping these components on a finite element mesh. Model functions for textures have individual height and individual full width at half maximum as a measure for the strength and scatter of the texture component they represent. In the formulation used for this study they have the form of central functions, i.e. their scatter is isotropic in orientation space. The reproduction of the orientation distribution function by such texture components can be expressed in terms of the superposition

$$f(g) = F + \sum_{c=1}^{C} I^c f^c(g) = \sum_{c=0}^{C} I^c f^c(g) \quad \text{where} \quad I^0 = F,\ f^0(g) = 1 \tag{1}$$

where g is the orientation, $f(g)$ is the orientation distribution function, and F is the volume portion of all randomly oriented crystals (random texture component). F may be understood as the intensity of the only *global* component used in the approximation, equivalent to $f^c(g) = 1$ for each orientation point in Euler space, $g \in G$. The intensity I^c describes the volume fraction of all crystallites belonging to the component c. The orientation density of the component is described by a central function, i.e. its value decreases isotropically with increasing orientation distance $\tilde{\omega}^c = \tilde{\omega}(g^c, g)$ from the maximum. This means that $f^c(g)$ only depends on $\tilde{\omega}^c = \tilde{\omega}(g^c, g)$, but it is independent on the rotation axis $\tilde{n}^c$. The orientation distribution function is defined by

$$f(g)\mathrm{d}g = 8\pi^2 \frac{\mathrm{d}V_g}{V} \text{ which implies } f(g) \geqslant 0 \tag{2}$$

where V is the sample volume and $\mathrm{d}V_g$ the volume of all crystals with an orientation g within the orientation portion $\mathrm{d}g = \sin(\phi)\mathrm{d}\phi\mathrm{d}\varphi_1\mathrm{d}\varphi_2$. Normalization requires

$$\oint f^c(g)\mathrm{d}g = 1 \text{ which implies } \sum_{c=0}^{C} I^c = 1 \tag{3}$$

As a rule texture components require positivity, i.e.

$$f^c(g) \geqslant 0 \quad \text{for all } g \in G \text{ and } I^c > 0 \tag{4}$$

where G is the orientation space.

Spherical central functions, including corresponding pole figures, can be written as series expansions of χ functions or, respectively, Legendre polynomials. More practical approximations of texture components have been introduced on the basis of spherical Gauss- and Lorentz-functions. The work presented in this study makes use of Gauss-shaped model functions for the decomposition of the orientation distribution function which are described by

$$f^c(g) = N^c \exp(S^c \cos\tilde{\omega}) \tag{5}$$

where

$$S^c = \frac{\ln 2}{1 - \cos(b^c/2)} \quad \text{and} \quad N^c = \frac{1}{I_0(S^c) - I_1(S^c)} \tag{6}$$

The corresponding projection of that component in a pole figure, $P_h(g^c, b^c, y)$, can be calculated in closed analytical form according to

$$P_h(g^c, b^c, y) = N^c \exp(S^c \sin(\upsilon^c/2)) I_0(S^c \cos(\upsilon^c/2)) \tag{7}$$

and

$$\cos \upsilon^c = h(g^c, y) \tag{8}$$

where υ^c describes the geometry of the component c in the respective pole figure projection and $I_l(x)$ the generalized Bessel functions. The index h in P_h indicates the lattice plane normal (in crystal coordinates) lying parallel (or antiparallel) to the scattering vector y. The scattering direction y is usually also referred to as *sample* direction since it is related to the sample coordinate system. The value b^c is the half width and can be interpreted as the mean diameter of a spherical component in orientation space and g^c is the center orientation of the texture component [52,53]. The complete set of texture components which describes the underlying orientation distribution in the best way can be determined by solving a least squares problem of the deviation between the experimentally observed and the recalculated pole figures.

The texture component method is well suited for an incorporation of texture into crystal plasticity finite element models because it is based on sets of localized spherical normalized standard functions which are characterized by simple parameters of physical significance (Euler angle triple for the main orientations, volume fractions, full widths at half maximum). Typically only a few texture components are required to describe the orientation distribution function which in turn can represent the texture of any grain assembly whatever size it may have. The input textures can be obtained from any experimental or theoretical source.

The texture component method was originally introduced by Lücke et al. [52] and later improved by Helming [53]. The basic idea of using texture components, however, goes back to the early texture studies where experimental and predicted pole figures were mostly interpreted in terms of the evolution and physical significance of discrete texture components [17].

In Section 2.4 we will show how the texture components can be decomposed and mapped on a finite element grid in cases where the underlying constitutive model has an orientation dependent form.

2.3. The crystal plasticity constitutive model

In this study we use the constitutive crystal plasticity model suggested by Kalidindi et al. [43]. In this formulation one assumes the stress response at each continuum point to be potentially given by one crystal or by a volume-averaged response of a set of grains comprising the respective material portion. The latter assumption can be formulated as a local strain-rate homogenization assumption. In case of a multi-grain description the volume averaged stress amounts to

$$\langle \mathbf{T} \rangle = \sum_{k=1}^{N} (w_k \mathbf{T}_k) \tag{9}$$

where N is the total number of individual orientations mapped onto an integration point using the Taylor assumption, w_k the volume fraction of each single orientation extracted from a texture component as described above, $\mathbf{T}_k$ the Cauchy stress produced by the kth individual orientation, and $\langle \mathbf{T} \rangle$ the volume average stress produced by all orientations mapped at the integration point. The constitutive equation for the stress in each grain is then expressed in terms of

$$\mathbf{T}^* = \mathbf{C}\mathbf{E}^* \tag{10}$$

where $\mathbf{C}$ is the fourth-order elastic tensor and $\mathbf{E}^*$ an elastic strain measure,

$$\mathbf{E}^* = \frac{1}{2}(\mathbf{F}^{*\mathrm{T}}\mathbf{F}^* - 1) \tag{11}$$

obtained by the polar decomposition of the deformation gradient,

$$\mathbf{F}^* = \mathbf{F}\mathbf{F}^{\mathrm{p}} \tag{12}$$

with $\det(\mathbf{F}^*) > 0$ and $\det(\mathbf{F}^{\mathrm{p}}) = 1$. While the former constraint for the determinant of the elastic part of the deformation gradient, $\det(\mathbf{F}^*) > 0$, means that elastic volume changes are admissible the latter constraint on the determinant $\det(\mathbf{F}^{\mathrm{p}})$ refers to the reasonable assumption of plastic incompressibility.

The stress measure is the elastic work conjugate to the strain measure $\mathbf{E}^*$,

$$\mathbf{T}^{*} = \mathbf{F}^{*-1}(\det(\mathbf{F}^{*})\mathbf{T})(\mathbf{F}^{*})^{-\mathrm{T}} \tag{13}$$

where $\mathbf{T}$ is the symmetric Cauchy stress tensor in the grain, and $\mathbf{F}^{*}$ is a local elastic deformation gradient defined in terms of the local *total* deformation gradient $\mathbf{F}$ and the local *plastic* deformation gradient $\mathbf{F}^{\mathrm{p}}$. The plastic deformation gradient is given by the flow rule

$$\dot{F}^{\mathrm{p}} = \mathbf{L}^{\mathrm{p}}\mathbf{F}^{\mathrm{p}} \tag{14}$$

with the velocity gradient

$$\mathbf{L}^{\mathrm{p}} = \sum_{k=1}^{N} \dot{\gamma}_k m_k, m_k = \hat{b}_k \otimes \hat{n}_k \tag{15}$$

where m_k are the kth dyadic slip products of unit vectors $\hat{b}_k$ in the slip direction and $\hat{n}_k$ normal to the slip plane, and $\dot{\gamma}_k$ the shear rates on these systems. The specific constitutive functions for the plastic shearing rates $\dot{\gamma}_k$ on the slip systems are taken as

$$\dot{\gamma}_k = \dot{\gamma}_o \left| \frac{\tau_k}{\tau_{k,\mathrm{crit}}} \right|^{\frac{1}{m}} \mathrm{sgn}(\tau_k) \tag{16}$$

where τ_k is the resolved shear stress for the slip system k, and $\tau_{k,\mathrm{crit}}$ is the actual critical shear stress on the kth slip system. $\dot{\gamma}_0$ is a reference value of the slip rate and m represents the strain rate sensitivity parameter. The calculation of $\tau_{k,\mathrm{crit}}$ is obtained by accounting for latent hardening through the use of an appropriate hardening matrix where the evolution of the slip system resistance during deformation can be taken as

$$\tau_{k,\mathrm{crit}} = \sum_{i} h^{ki}|\dot{\gamma}^{i}|, \quad h^{ki} = q^{ki}h^{(i)},$$
$$h^{(i)} = h_0\left\{1 - \frac{s^{i}}{s_s}\right\}^{a} \tag{17}$$

where h^{ki} is the rate of strain hardening on the kth slip system due to the shear rate, $\dot{\gamma}^{i}$, on the ith slip system, q^{ki} are the components of a matrix which describes the latent hardening behavior of the crystal, and $h^{(i)}$ is the hardening rate of the single slip system i. The hardening rate can be fitted by using s_s as a saturation parameter, and h_0 and a as adjustable parameters [54]. The values of h_0, a, and s_s are taken to be identical for all slip systems. The matrix h^{ki} assumes the form

$$h^{ki} = \begin{bmatrix} A & qA & qA & qA \\ qA & A & qA & qA \\ qA & qA & A & qA \\ qA & qA & qA & A \end{bmatrix} \tag{18}$$

where q is the ratio of the latent hardening rate to the self-hardening rate, and A is a 3×3 matrix populated by ones.

In the present study, 24 slip systems with crystallographic $\langle 1\,1\,0\rangle$ slip directions and $\{1\,1\,1\}$ as well as $\{1\,1\,2\}$ slip planes are taken into account for room temperature simulations of ferritic, i.e. body-centered-cubic steels.

2.4. Using texture components in a crystal plasticity finite element simulation

The main task of the new concept is to represent sets of spherical Gaussian texture components on the integration points of a finite element mesh for a crystal plasticity simulation. This procedure works in two steps, Fig. 1. First, the discrete preferred orientation g^{c} (center orientation, mean orientation) is extracted from each of the texture components and assigned in terms of its respective Euler triple $(\varphi_1, \phi, \varphi_2)$, i.e. in the form of a *single* rotation matrix, onto *each* integration point. This step corresponds to the creation of a perfect single crystal. In the second step, these discrete orientations are re-oriented in such a fashion that their resulting overall distribution reproduces the texture function which was originally prescribed in the form of a Gaussian texture component. In other words the orientation scatter described initially by a texture component function is in the finite element mesh represented by a systematically re-oriented set of orientations, each assigned to one integration point, which reproduces the original spherical scatter prescribed by that component.

This means that the scatter which was originally only given in orientation space is now represented by a distribution both, in real space and in orientation space, i.e. the initial spherical distribution is transformed into a spherical *and* lateral distribution. The described allocation and re-orientation procedure is formulated as a weighted sampling Monte Carlo integration scheme in Euler space.

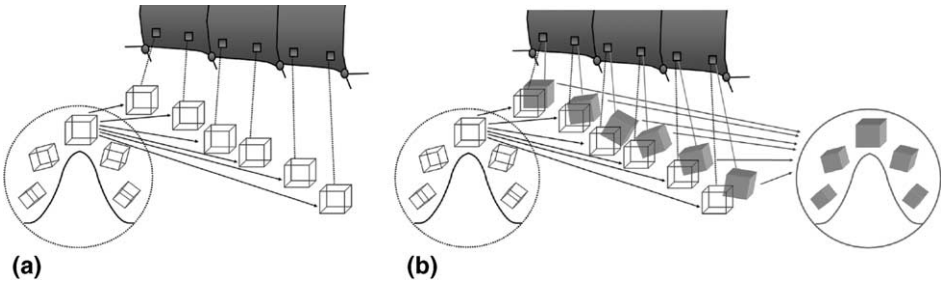

Fig. 1. Schematical presentation of the two steps required for mapping a texture component on the integration points: (a) in the first step the preferred orientation g^c (center orientation) of each texture component is assigned onto *each* integration point and (b) in the second step the orientations are re-oriented in such a way that their distribution reproduces the texture function which was originally prescribed in the form of a Gaussian texture component.

It is an important detail that the use of the Taylor assumption locally allows one to map more than one preferred crystallographic orientation on each integration point and to assign to each of them an individual volume fraction. This means that the procedure of mapping and rotating single orientations in accord with the initial texture component scatter width is individually conducted for *all* prescribed components as well as for the random background extracted from initial experimental or theoretical data.

After decomposing and representing the initial texture components as a lateral and spherical single orientation distribution in the mesh, the texture *component* concept is no longer required in the further procedure. This is due to the fact that during the subsequent crystal plasticity finite element simulation each individual orientation originally pertaining to one of the texture components which were initially mapped on the finite element mesh can undergo an *individual* orientation change as in the conventional crystal plasticity methods. This means that the texture component method loses its significance during the simulation. In order to avoid confusion one should, therefore, underline that the texture component method is used to *feed* textures into finite element simulations on a strict physical and quantitative basis. The *components* as such, however, are in their original form as compact functions not tracked during the simulation, but only the individual orientation fractions which compose them. It must also be noted that the orientation points which were originally obtained from the components do not represent individual *grains* but portions of an orientation distribution function.

3. Set-up of the finite element model and simulation details

3.1. Finite element model

The finite element calculations were conducted by using MSC/Marc in conjunction with the user defined material subroutine HYPELA2 [55]. An implicit crystal plasticity procedure developed by Kalidindi et al. [43] was implemented and used for the time integration of the constitutive equations. Hardening of the ferritic low carbon body-centered-cubic steel was described in terms of a set of adjustable parameters, i.e. $\dot{\gamma}_0 = 0.001\ \mathrm{s}^{-1}$ was used as reference value for the slip rate. The strain rate sensitivity parameter m was taken as 0.05. As hardening matrix parameters we used $q^{\alpha\beta} = 1.0$ for coplanar slip systems and $q^{\alpha\beta} = 1.4$ for non-coplanar systems. The components of the elasticity tensor (pure single crystalline Fe) were taken as $C_{11} = 230.1$ GPa, $C_{12} = 134.6$ GPa, and $C_{44} = 116.6$ GPa. The values of the slip system hardening parameters h_0, a, and s_s, and the initial value of the slip resistance s_0 were taken to be $h_0 = 180$ MPa, $s_s = 148$ MPa, $a = 2.25$, and $s_0 = 16$ MPa. The potential slip system families are the 12 $\{111\}\langle 111\rangle$ and the 12 $\{112\}\langle 111\rangle$ systems.

Fig. 2a shows the geometry of the tools used in the simulation. Due to the orthotropic sample

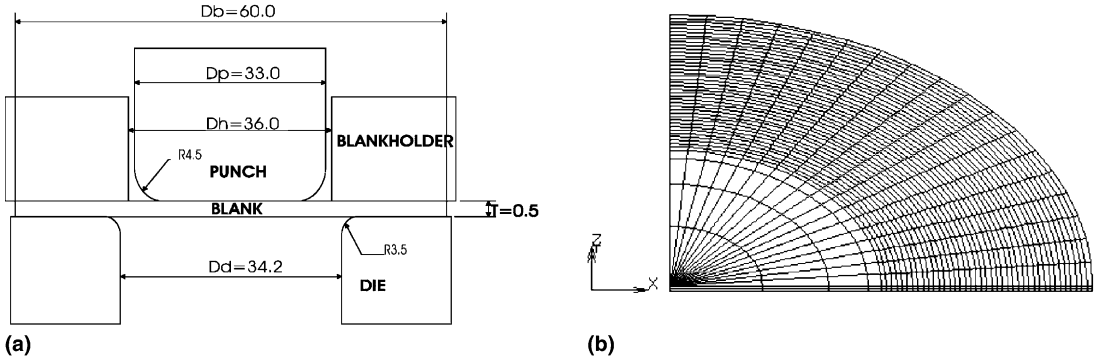

Fig. 2. (a) Finite element model showing the geometry of the tools in units of mm and (b) mesh configuration.

symmetry of the deformation problem, only a quarter of the blank was modeled. A set of 1584 eight-node brick elements was used to discretize the sample. Fig. 2b shows the mesh configuration of the specimen. The Coulomb friction coefficient was assumed to be $\mu = 0.1$ between the punch and the blank. With these parameters each simulation run required about 4–8 h of CPU time on a UNIX single processor workstation.

3.2. Investigated texture components and random texture

The texture components which typically occur with notable volume fractions in rolled and subsequently heat treated body centered cubic steel sheets [22,23] are the $\{0\,0\,1\}\langle 1\,1\,0\rangle$ or 45° about the normal rotated cube component ($\varphi_1 = 0°$, $\phi = 0°$, $\varphi_2 = 45°$), the $(1\,1\,1)[1\,\bar{1}\,0]$ component ($\varphi_1 = 0°$, $\phi = 54.7°$, $\varphi_2 = 45°$), and the $(1\,1\,1)[1\,1\,\bar{2}]$ component ($\varphi_1 = 90°$, $\phi = 54.7°$, $\varphi_2 = 45°$). While the $\{1\,1\,1\}\langle u\,v\,w\rangle$ texture components are the two most relevant orientations emerging during primary recrystallization the $(0\,0\,1)[1\,1\,0]$ component is inherited from rolling owing to pronounced recovery [55,57]. Another important texture component often resulting from recrystallization is the $\varphi_1 = 15°$, $\phi = 45°$, $\varphi_2 = 50°$ ($\approx (5\,5\,7)[5\,8\,\underline{3}]$) orientation which is about 10° off the $\{1\,1\,1\}\langle u\,v\,w\rangle$ fiber [22,23] (all Euler triples are given in Bunge notation [57].)

The texture component crystal plasticity finite element simulations in this study are conducted by using combinations of the texture components given above (with 7° and with 15° full width at half maximum) with a random background component, Table 1. The incorporation of the random portion of the starting texture in the form of a pseudo-component may be important [16,48] because random *starting* textures do, as a rule, not necessarily *remain* random during forming. As any other orientation, randomly distributed orientations may gradually reorient during the forming process and enhance or smoothen anisotropy as a result of texture evolution. Although the contribution of the random pseudo-component is of course an isotropic one in the *beginning* of deformation it may evolve into an anisotropic one *during* deformation.

The random background texture component is in principle assigned to the integration points in the same way as the regular ideal texture components. This means that in the current study each integration point is described by one rotation matrix which is selected randomly from the set of spherical orientation component functions (typical texture components) and a second rotation matrix which is generated as a random orientation. Like the prescribed ideal texture components, the random texture component does cease to exist as a *component* in the further simulation procedure [47]. This is due to the fact that during the subsequent crystal plasticity finite element simulation each individual pair of orientations, originally pertaining to one of the texture components and to the random component, can undergo an *individual* orientation change as in the conventional crystal plasticity methods [40–43].

Table 1
Texture components and orientation scatter used as starting conditions in the simulations

Ideal texture component					Random texture component	
φ_1 [°]	ϕ [°]	φ_2 [°]	Scatter width [°]	Volume fraction [%]	Orientation	Volume fraction [%]
0	54.7	45	7 and 15	80	Random	20
90	54.7	45	7 and 15	80	Random	20
15	45	50	7 and 15	80	Random	20
0	0	45	7 and 15	80	Random	20

Owing to the orthorhombic sample symmetry each of the single orientations has in the starting texture to be balanced by three additional symmetrically equivalent orientations in order to correctly reproduce the response of the material in the crystal plasticity finite element calculations. Consequently, each of the symmetrical variants was assigned one quarter of the volume of the original component, i.e. 20 vol.% of the total volume at one integration point. The remaining 20 vol.% is occupied by the randomly selected orientation. This initial symmetry operation is required since the starting data which are typically taken from experimental X-ray data do not allow one to differentiate between the different symmetrical variants of a texture component owing to Friedel's law and to the symmetry group of the sample coordinate system.

4. Results and discussion

4.1. Simulations

Fig. 3 shows the simulated ear profiles for the four individual texture components together with the random component for different scatter widths. Cup drawing of the two $\{1\,1\,1\}\langle u\,v\,w\rangle$ texture components ($\varphi_1 = 0°$, $\phi = 54.7°$, $\varphi_2 = 45°$ and $\varphi_1 = 90°$, $\phi = 54.7°$, $\varphi_2 = 45°$, respectively) leads in either case to a six-ear profile. This type of shape is principally in accordance with earlier studies. It can be explained in terms of the corresponding symmetry of the Schmid tensors of the $\{1\,1\,1\}\langle u\,v\,w\rangle$ texture components. While a specific $\{1\,1\,1\}\langle u\,v\,w\rangle$ orientation has a threefold symmetry at the beginning of loading (see schematical drawing in Fig. 4a) the addition of the other three symmetrical equivalent orientations results in an altogether sixfold symmetry, Fig. 4b. The fact that the 6 ears do not reach the same height, as predicted by homogenization theory, may be attributed to the effect of texture evolution occurring during forming. This observation suggests that both, the incorporation of a random background component and the use of a crystal plasticity method allowing for texture update, are necessary ingredients in such simulations.

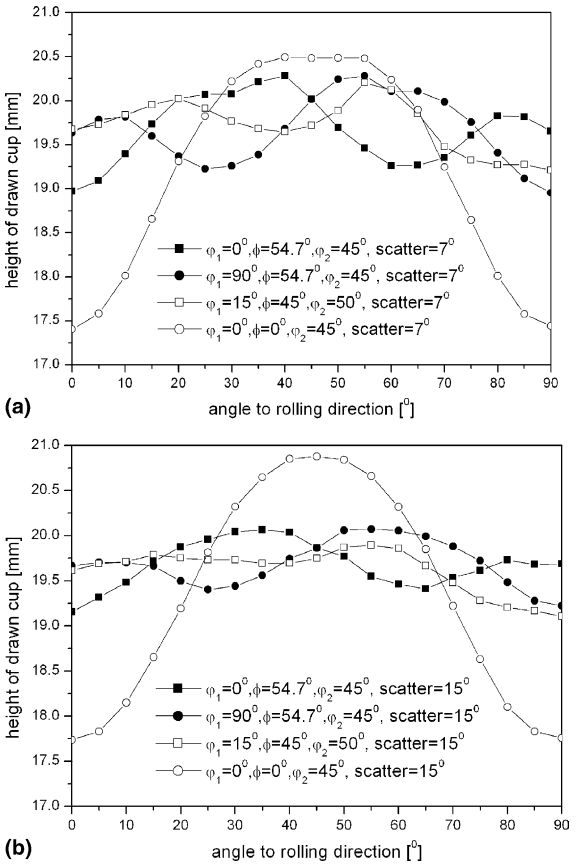

Fig. 3. Ear profiles of individual texture components with: (a) scatter width 7° and (b) scatter width 15°.

The course of the ear profiles (for both scatter widths) of the $(1\,1\,1)[1\,\bar{1}\,0]$ component ($\varphi_1 = 0°$, $\phi = 54.7°$, $\varphi_2 = 45°$) shows a mirror symmetrical shape relative to 45° to those of the $(1\,1\,1)[1\,1\,\bar{2}]$ component ($\varphi_1 = 90°$, $\phi = 54.7°$, $\varphi_2 = 45°$), Fig. 3a and b. This symmetry can be explained in terms of some simple considerations about those $\langle 1\,1\,1\rangle$ slip directions which predominantly determine the deformation of $\{1\,1\,1\}\langle uvw\rangle$ texture components in body centered steel sheets, Fig. 4a: The two texture components $(1\,1\,1)[1\,\bar{1}\,0]$ and $(1\,1\,1)[1\,1\,\bar{2}]$ have a 30° rotation relationship among each other when rotated about their common [1 1 1] normal direction. Each of the two texture components has three dominant active slip directions as indicated by the projected arrows in the top row of Fig. 4b. The initial symmetry operations explained above, which add to each orientation at an integration point three symmetrical equivalents (in the case of orthorhombic sample symmetry),

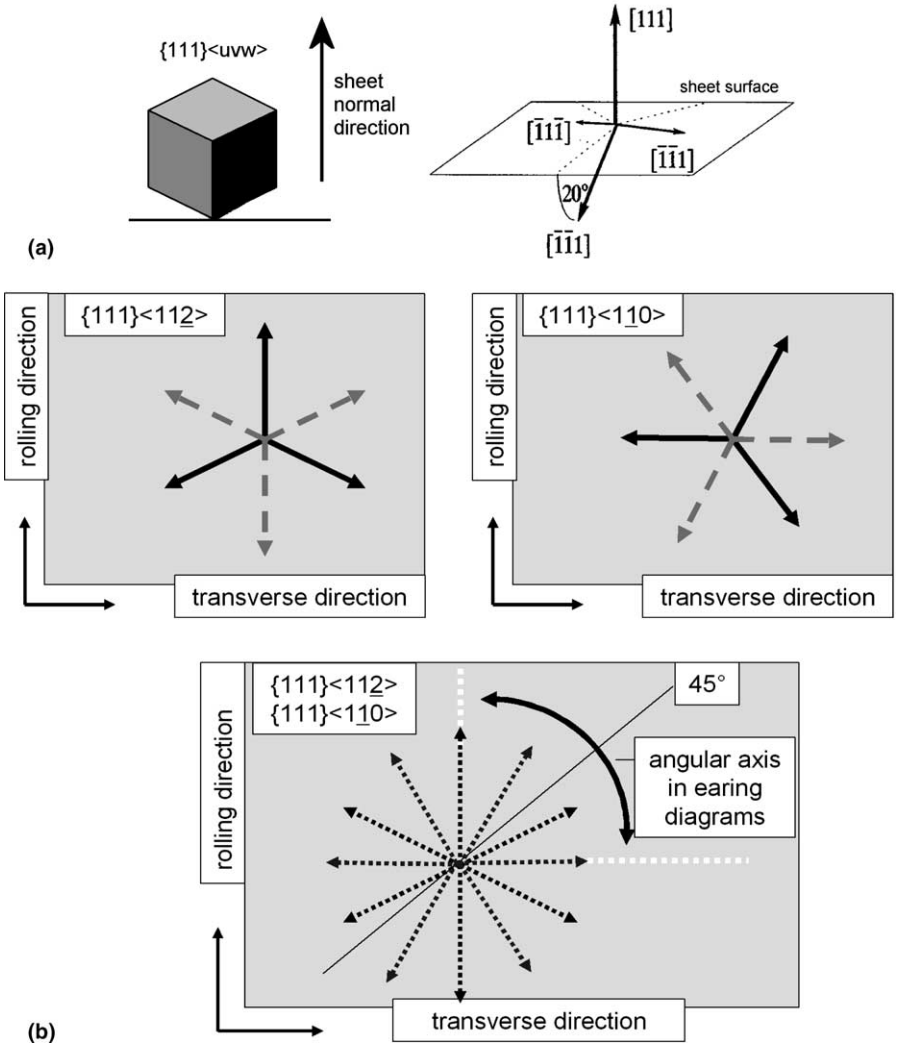

Fig. 4. Schematical diagram with some important symmetries: (a) of projected $\langle 1\,1\,1\rangle$ slip directions which are relevant for earing and cup drawing of body centered cubic materials and (b) the slip arrows are projected into the rolling plane assuming a top view position.

contributes three more dominant active slip directions to each Gauss point (see dotted gray arrow projections in the upper row of Fig. 4b). The resulting configuration for the two $\{1\,1\,1\}\langle u\,v\,w\rangle$ texture components then reveals a 45° symmetry relationship as indicated by the sketch in the bottom row of Fig. 4b. This symmetry effect induced by the predominant $\langle 1\,1\,1\rangle$ slip directions is actually visible in Fig. 3a and b.

In the six ear profiles of the two $\{1\,1\,1\}\langle u\,v\,w\rangle$ texture components not all ears have the same height, i.e. two sets of three (symmetrically similar) ears differ from each other both in terms of height and shape. Figs. 3b, 5a and b reveal that this effect is smoothened when the scatter width (full width at half maximum) of the initial texture components is increased from 7° (Fig. 3a) to 15° (Fig. 3b). The texture component $\varphi_1 = 15°$, $\phi = 45°$, $\varphi_2 = 50°$ leads to eight ears. Figs. 3a and 5c show that two sets of ears exist with different height and shape. The rotated cube component, $\varphi_1 = 0°$, $\phi = 0°$, $\varphi_2 = 45°$, $(0\,0\,1)[1\,1\,0]$, reveals only four huge ears along the rim of the drawn cup. Fig. 5d shows that an increase in the initial orientation scatter for the texture component, results also in an increase of the ear height.

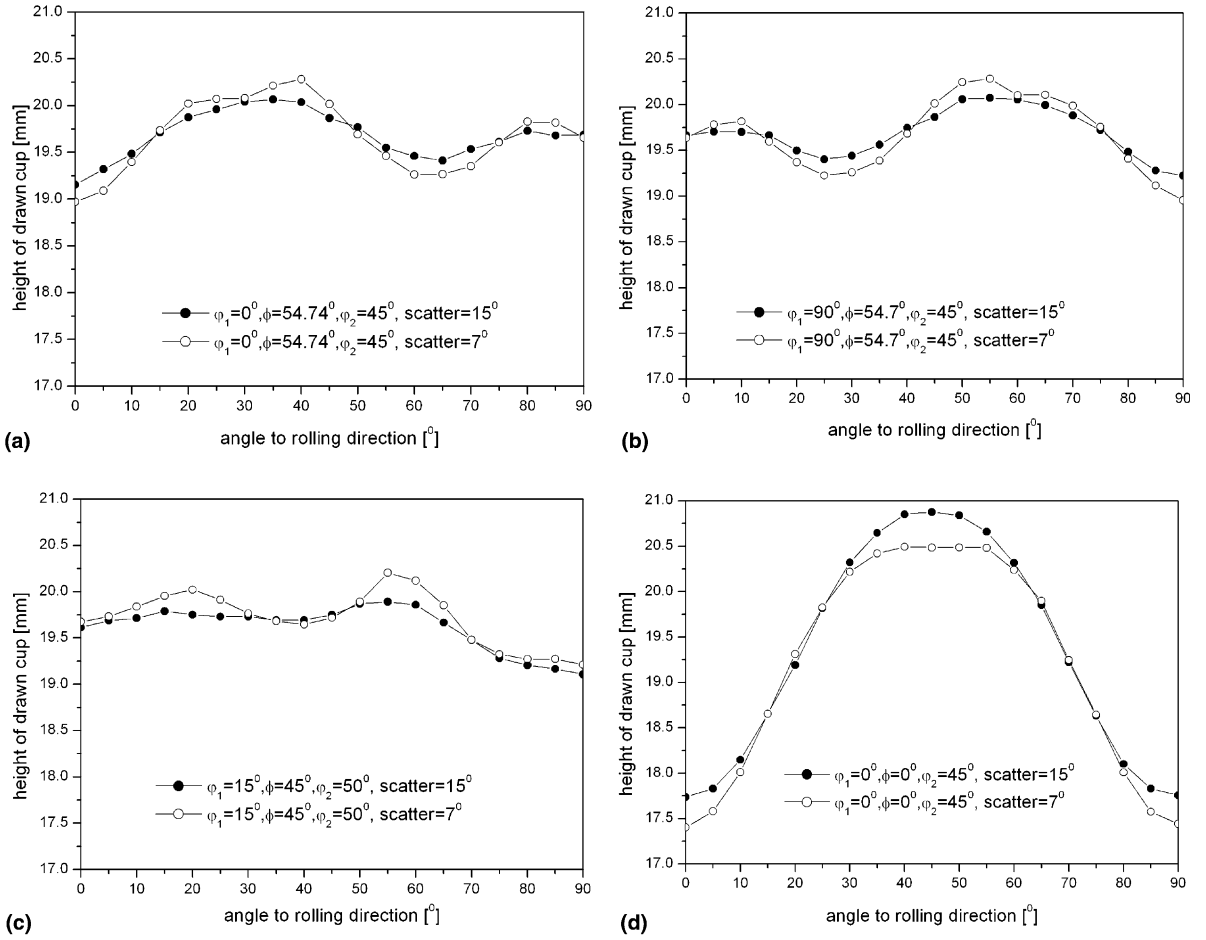

Fig. 5. Influence of the spherical scatter width of the texture components on the resulting ear profiles: (a) $\varphi_1 = 0°$, $\phi = 54.7°$, $\varphi_2 = 45°$, $(1\,1\,1)[1\,\bar{1}\,0]$; (b) $\varphi_1 = 90°$, $\phi = 54.7°$, $\varphi_2 = 45°$, $(1\,1\,1)[1\,1\,\bar{2}]$, (c) $\varphi_1 = 15°$, $\phi = 45°$, $\varphi_2 = 50°$, $\approx(5\,5\,7)[5\,8\,\underline{3}]$ and (d) $\varphi_1 = 0°$, $\phi = 0°$, $\varphi_2 = 45°$, $(0\,0\,1)[1\,1\,0]$.

The presented ear profiles of the four individual texture components suggest that they essentially reproduce the symmetry of the crystallography of the center orientation relative to the sheet and forming symmetry.

According to the rim shapes characteristic differences occur in ear height for the various starting textures. The $\varphi_1 = 0°$, $\phi = 0°$, $\varphi_2 = 45°$ component clearly shows a maximum variation in the ear height along the cup rim. This means that this texture component is very detrimental with respect to the in-plane isotropy of formed steels. Owing to its large impact on the overall shape anisotropy and its fourfold symmetry its effect on the yield anisotropy cannot be easily compensated. Such compensation, which is for instance exploited in the field of aluminum forming [16], would require texture components with a shape anisotropy which is inverse to that of the $\varphi_1 = 0°$, $\phi = 0°$, $\varphi_2 = 45°$ component. However, such orientations do not exist in typcial textures of rolled and annealed steel sheets [18–23]. The conclusion from that is that the $\varphi_1 = 0°$, $\phi = 0°$, $\varphi_2 = 45°$ texture component must be avoided in sheet steels which are subject to subsequent cup drawing operations.

The ear profile generated by the $\varphi_1 = 0°$, $\phi = 54.7°$, $\varphi_2 = 45°$ and $\varphi_1 = 90°$, $\phi = 54.7°$, $\varphi_2 = 45°$ texture components is much smoother when compared to that of the 45° rotated cube orientation. Furthermore, the occurrence of the two texture components with the same volume fraction together in one sheet leads to a perfect isotropic shape owing to their 30° $\langle 1\,1\,1\rangle$ rotational or respectively 45° mirror equivalence, i.e. the planar anisotropy would be zero for such a case.

4.2. Recommendations with respect to texture design of body-centered-cubic steel sheets

It is well known that recrystallization in body-centered-cubic steel sheets is not homogeneous but highly orientation dependent [17–23,55–58]. Both, the kinetics and the resulting grain morphology considerably depend on the deformation texture. This is in particular true for the strongest or second-strongest cold rolling texture component $\{0\,0\,1\}\langle 1\,1\,0\rangle$ ($\varphi_1 = 0°$, $\phi = 0°$, $\varphi_2 = 45°$) [55,57]. Recrystallization in such grains can be delayed in case of a small and even suppressed in case of a larger grain size [55,57,59,60]. Also, the presence of small precipitations on the grain boundaries can play an important role in that context. This allows for strong recovery of grains with a $\{0\,0\,1\}\langle 1\,1\,0\rangle$ orientation in sheet steels. Even at the final stage of recrystallization $\{0\,0\,1\}\langle 1\,1\,0\rangle$ oriented crystals do often not reveal a sufficient number of recrystallization nuclei inside their grain borders. More typically recrystallization in $\{0\,0\,1\}\langle 1\,1\,0\rangle$ oriented grains occurs by newly formed crystals entering from neighboring grains. This substantial reluctance of $\{0\,0\,1\}\langle 1\,1\,0\rangle$ oriented crystals against recrystallization is often enhanced by the fact that certain amounts of this texture component are inherited from the final hot rolling steps due to (planned or unplanned) insufficient austenitization. In sum it is, therefore, sensible to avoid the occurrence of this texture component in annealed body-centered-cubic steel sheets. The opposite is true for the $\{1\,1\,1\}\langle u\,v\,w\rangle$ texture fiber. The recrystallization behavior of these grains has been the subject of a number of thorough studies in the past [17–23]. Owing to the predicted ear profiles discussed above an optimum shape isotropy can be achieved by a one-to-one mixture of the two main texture components $(1\,1\,1)[1\,\bar{1}\,0]$ and $(1\,1\,1)[1\,1\,\bar{2}]$.

5. Conclusions

We used a texture component crystal plasticity finite element method to investigate the effect of texture on the earing behavior in body-centered-cubic steel sheets. The conclusions are:

1. The ear profiles depend strongly on the respective texture component: The two $\{1\,1\,1\}\langle u\,v\,w\rangle$ texture components ($\varphi_1 = 0°$, $\phi = 54.7$, $\varphi_2 = 45°$ and $\varphi_1 = 90°$, $\phi = 54.7°$, $\varphi_2 = 45°$) lead to six ears. The texture component $\varphi_1 = 15°$, $\phi = 45°$, $\varphi_2 = 50°$ leads to eight ears. The presence of the rotated cube component, $\varphi_1 = 0°$, $\phi = 0°$, $\varphi_2 = 45°$, leads to four huge ears.
2. An increase in the number of ears entails a drop in the ear height.

3. An increase in the orientation scatter of the texture component before deformation does not generally lead to a drop in the resulting shape anisotropy.
4. Owing to its large in-plane anisotropy the rotated cube component (which may result from pronounced recovery) should be avoided as a main texture component in body-centered-cubic steel sheets.
5. In principal the incorporation of a random texture component prior to mechanical loading is useful in order to properly account for anisotropy which arises from texture evolution effects during forming. In the present case, however, texture evolution of that random component seems to be of minor importance for the final earing profile.
6. The texture component finite element method can be used as an engineering numerical laboratory which helps the user to decide which forming situations require the direct incorporation of texture including texture update and which do not. Also, it can be used to derive phenomenological constitutive data as input parameters for instance for yield surface simulations. We assume that future commercial applications of anisotropy theory in conjunction with industry-scale forming and tool design simulations will make increasingly use of the texture component crystal plasticity finite element method owing to its physically-based foundations and the ever-decreasing costs associated with CPU time.

Acknowledgements

The authors are grateful to the Deutsche Forschungsgemeinschaft DFG (German Research Foundation) which is funding this study within the Schwerpunktprogramm 1138 (Modellierung von Größeneinflüssen bei Fertigungsprozessen).

References

[1] P. Van Houtte, K. Mols, B. Van Bael, E. Aernoudt, Text. Microstruct. 11 (1989) 23.
[2] W.F. Hosford, The Mechanics of Crystals and Textured Polycrystals, Oxford University Press, 1993.
[3] B. Bacroix, P. Gilormini, Model. Simul. Mater. Sci. Eng. 3 (1995) 1.
[4] S. Balasubramanian, L. Anand, Computat. Mech. 17 (1996) 209.
[5] W.F. Hosford, Text. Microstruct. 26 (1996) 479.
[6] U.F. Kocks, C.N. Tóme, H.R. Wenk, Texture and Anisotropy—preferred Orientations in Polycrystals and Their Effect on Material Properties, Cambridge University Press, 1998.
[7] Y. Zhou, J.J. Jonas, J. Savoie, A. Makinde, S.R. MacEwen, Int. J. Plast. 14 (1998) 117.
[8] J.G. Hu, J.J. Jonas, T. Ishikawa, Mater. Sci. Eng. A 256 (1998) 51.
[9] H. Aretz, R. Luce, M. Wolske, R. Kopp, M. Goerdeler, V. Marx, G. Pomana, G. Gottstein, Model. Simulat. Mater. Sci. Eng. 8 (2000) 881.
[10] B. Peeters, E. Hoferlin, P. Van Houtte, E. Aernoudt, Int. J. Plast. 17 (2001) 819.
[11] R. Becker, R.E. Smelser, S. Panchanadeeswaran, Model. Simulat. Mater. Sci. Eng. 1 (1993) 203.
[12] A.J. Beaudoin, P.R. Dawson, K.K. Mathur, U.K. Kocks, D.A. Korzekwa, Comput. Methods Appl. Mech. Eng. 117 (1994) 49.
[13] O. Engler, S. Kalz, Mater. Sci. Eng. A 373 (2004) 350.
[14] Y.H. Chung, K.K. Cho, J.H. Han, M.C. Shin, Scr. Mater. 43 (2000) 759.
[15] J. Savoie, Y. Zhou, J.J. Jonas, S.R. MacEwen, Acta Mater. 44 (1996) 587.
[16] Z. Zhao, W. Mao, F. Roters, D. Raabe, Acta Mater. 52 (2004) 1003.
[17] G. Wassermann, J. Grewen, Texturen metallischer Werkstoffe (in German), 1969, Springer-Verlag, Berlin, Germany.
[18] S. Mishra, C. Därmann, K. Lücke, Acta Metall. 32 (1984) 2185.
[19] W.B. Hutchinson, Int. Mater. Rev 29 (1984) 25.
[20] U. von Schlippenbach, F. Emren, K. Lücke, Acta Metall. 34 (1986) 1289.
[21] R. Ray, J. Jonas, Mater. Rev. 35 (1990) 1.
[22] M. Hölscher, D. Raabe, K. Lücke, Steel Res. 62 (1991) 567.
[23] D. Raabe, K. Lücke, Mater. Sci. Technol. 9 (1993) 302.
[24] R. Hill, Proc. R. Soc. London A193 (1948) 281.
[25] R. Hill, Math Proc. Cambridge Philos. Soc. 85 (1949) 179.
[26] WF Hosford, N. Seventh, in: American Metal Working Research Conference Proceedings, 1979, p. 191.
[27] F. Barlat, Mater. Sci. Eng. 91 (1987) 55.
[28] F. Barlat, J. Lian, Int. Int. J. Plast. 5 (1989) 51.
[29] D. Banabic, H.J. Bunge, K. Pöhlandt, A.E. Tekkaya, Formability of Metallic Materials, Springer-Verlag, Berlin, Heidelberg, 2000.
[30] H.J. Bunge, Krist. Tech. 5 (1970) 145.
[31] A. Van Bael, P. Von Houtte, E. Aernoudt, F.R. Hall, I. Pillinger, P. Hartley, C.E.N. Sturgess, Text. Microstruct. 14–18 (1991) 1007.

[32] P. Van Houtte, A. Van Bael, J. Winters, E. Aernoudt, F.R. Hall, N. Wang, I. Pillinger, P. Hartley, C.E.N. Sturgess, in: S.I. Andersen, J.B. Bilde-Sorensen, N. Hansen, D. Jul Jensen, T. Leffers, H. Liholt, T. Lorentzen, O.B. Pedersen, B. Ralph (Eds.), Proceedings of the 13th RISO International Symposium on Metallurgy and Materials Science: Modeling of Plastic Deformation and It's Engineering Applications, Riso National Laboratory, Roskilde, 1992, p. 161.
[33] S. Li, E. Hoferlin, A. Van Bael, P. Van Houtte, Adv. Eng. Mater. 3 (2001) 990.
[34] S. Li, E. Hoferlin, A. Van Bael, P. Van Houtte, C. Teodosiu, Int. J. Plast. 19 (2003) 647.
[35] D. Raabe, P. Klose, B. Engl, K.P. Imlau, F. Friedel, F. Roters, Adv. Eng. Mater. 4 (2002) 169.
[36] B. Beckers, P. Pomana, G. Gottstein, P. Klimanek, M. Seefeld, Simulationstechniken in der Materialwissenschaft, Freiburger Forschungshefte, vol. 295, 1999, Technical Universität Freiburg, p. 209.
[37] B. Beckers, G. Pomana, G. Gottstein, in: A.S. Khan (Ed.), Proceedings of Conference on Constitutive and Damage Modeling of Inelastic Deformation and Phase Transformations, Neat Press, Fulton; MD, 1998, p. 305.
[38] S. Li, Y. Zhang, G. Gottstein, ISIJ Int. 39 (1999) 501.
[39] D. Pierce, R.J. Asaro, A. Needleman, Acta Metall. 30 (1982) 1087.
[40] R.J. Asaro, Adv. Appl. Mech 23 (1983) 1.
[41] D. Pierce, R.J. Asaro, A. Needleman, Acta Metall. 31 (1983) 1951.
[42] A. Needleman, R.J. Asaro, Acta Metall. 33 (1985) 923.
[43] S.R. Kalidindi, C.A. Bronkhorst, L. Anand, J. Mech. Phys. Solids 40 (1992) 537.
[44] K.K. Mathur, P.R. Dawson, Int. J. Plast. 5 (1989) 67.
[45] R.E. Smelser, R. Becker, ABAQUS User's Group Conference Proceedings, Oxford 1999, p. 457.
[46] A.J. Beaudoin, P.R. Dawson, K.K. Mathur, U.F. Kocks, D.A. Korzekwa, Comput. Methods Appl. Mech. Eng. 117 (1994) 49.
[47] D. Raabe, F. Roters, Int. J. Plast. 20 (2004) 339.
[48] D. Raabe, Z. Zhao, F. Roters, Scr. Mater. 50 (2004) 1085.
[49] E. Nakamachi, C.L. Xie, M. Harimoto, Int. J. Mech. Sci. 43 (2001) 631.
[50] C.L. Xie, E. Nakamachi, Mater. Des. 23 (2002) 59.
[51] D. Raabe, M. Sachtleber, Z. Zhao, F. Roters, S. Zaefferer, Acta Mater. 49 (2001) 3433.
[52] K. Lücke, J. Pospiech, J. Jura, J. Hirsch, Z. Metall. 77 (1986) 312.
[53] K. Helming, R.A. Schwarzer, B. Rauschenbach, S. Geier, B. Leiss, H. Wenk, K. Ullemeier, J. Heinitz, Z. Metall. 85 (1994) 545.
[54] Y. Wang, D. Raabe, C. Klüber, F. Roters, Acta Mater. 52 (2004) 2229.
[55] MSC. Marc User's Manual, Vol. D, MSC Software Corporation, 2001.
[56] D. Raabe, Steel Research 66 (1995) 222.
[57] D. Raabe, Scr. Metall. 33 (1995) 735.
[58] H.J. Bunge, Texture Analysis in Materials Science, Butterworths, London England, 1982.
[59] A. Martínez-de-Guerenu, F. Arizti, M. Díaz-Fuentes, I. Gutiérrez, Acta Mater. 52 (12) (2004) 3657–3664.
[60] A. Martínez-de-Guerenu, F. Arizti, I. Gutiérrez, Acta Mater. 52 (12) (2004) 3665–3670.